

引用格式: MING Ming, CHEN Tao, XU Tian-shuang. Vehicular Daytime High-resolution Imaging System Based on Phase-diversity Technology[J]. *Acta Photonica Sinica*, 2019, 48(3): 0312003

明名, 陈涛, 徐天爽. 基于相位差异技术的车载白天高分辨成像系统[J]. 光子学报, 2019, 48(3): 0312003

# 基于相位差异技术的车载白天高分辨成像系统

明名<sup>1,2</sup>, 陈涛<sup>1,2</sup>, 徐天爽<sup>3</sup>

(1 中国科学院长春光学精密机械与物理研究所, 长春 130033)

(2 中国科学院大学, 北京 100049)

(3 吉林大学 机械与航空航天工程学院, 长春 130012)

**摘 要:** 在 1.2 m 车载望远镜的基础上, 通过机上折轴卡塞格林焦点, 将主光学系统与白天成像系统相连, 实现了白天高分辨成像. 该系统采用短波红外波段, 在精密跟踪的同时, 校正大气波前整体倾斜. 近红外波段的双通道成像系统, 通过在焦与离焦像面同时采集后, 利用相位差异技术来提高成像分辨率. 该系统探测能力达到 5 等星, 成像分辨率接近两倍衍射极限, 观测时间比自适应系统延长 6 h.

**关键词:** 车载式; 光学望远镜; 光学设计; 成像分辨率; 相位测量

中图分类号: TH75

文献标识码: A

doi: 10.3788/gzxb20194803.0312003

## Vehicular Daytime High-resolution Imaging System Based on Phase-diversity Technology

MING Ming<sup>1,2</sup>, CHEN Tao<sup>1,2</sup>, XU Tian-shuang<sup>3</sup>

(1 *Changchun Institute of Optics, Fine Mechanics and Physics, Chinese Academy of Sciences, Changchun 130033, China*)

(2 *University of Chinese Academy of Sciences, Beijing 100049, China*)

(3 *School of Mechanical and Aerospace Engineering, Jilin University, Changchun 130012, China*)

**Abstract:** A bent Cassergrain focus was used to connect a daytime imaging system to a 1.2 m aperture vehicular telescope. The system employs a short-wavelength infrared waveband for precise tracking and corrects the global atmospheric wavefront tilt at the same time. Double-pass imaging is applied to the near-infrared waveband to produce the image, while the phase-diversity technique is used to restore the image resolution. The system can detect and correct objects with a magnitude 5 or less at an image resolution that is close to twice the diffraction limit. The observation time is 6 hours longer than that of the adaptive system.

**Key words:** Vehicular; Optical telescopes; Optical design; Imaging resolution; Phase measurement

**OCIS Codes:** 120.4820; 110.2970; 080.2740; 220.1140; 110.3000; 100.5070; 120.4570

## 0 Introduction

The imaging by an optical system mainly depends on the reflection of sunlight and thermal radiation of objects. Mainstream optical imaging systems with large apertures work in the visible or near-infrared

**Foundation item:** National High Technology Research and Development Program (No.2015AA8080333)

**First author:** MING Ming (1983—), male, associate research fellow, Ph.D Degree, mainly focuses on large aperture optical system. Email: 18987610@qq.com

**Contact author:** CHEN Tao (1965—), male, professor, Ph.D Degree, mainly focuses on optoelectronic precision tracking. Email: chent@ciomp.ac.cn

**Received:** Oct.14, 2018; **Accepted:** Dec.5, 2018

<http://www.photon.ac.cn>

region because this provides a higher optical resolution than the middle- and long-wavelength infrared regions with the same aperture. However, the effects of the sky background and atmosphere mean that these high-resolution imaging systems can only work when the observation station and target are at suitable relative positions, which is during sunrise and sunset. Thus, these imaging systems can work 4 h/day at most. New techniques and methods are needed for optical systems with large apertures to produce high-resolution images in the daytime<sup>[1-4]</sup>. To achieve short-exposure and high-resolution imaging, American scientists have designed a GEMINI system that uses phase-diversity technology<sup>[5-7]</sup> and is based on a 1.6 m aperture telescope, while CIOMP of Chinese Academy of Sciences applied lucky imaging and multi-band switching to achieve daytime imaging<sup>[8-10]</sup>. However, these two methods do not correct for the atmospheric wavefront distortion, which decreases the image resolution.

In order to improve the image resolution of an optical system, we considered a daytime high-resolution optical imaging system that is based on a bent Cassegrain focus and 1.2 m aperture telescope. The system design includes relay optics, a precise tracking and tilt correction system, and a short-exposure imaging system. High-resolution imaging in the daytime is achieved by correcting for the atmospheric wavefront tilt in the short-wavelength infrared band, performing a double pass in the near-infrared waveband, and applying phase-diversity technology for super-resolution on the wavefront. We verified the resolution capacity to be near the diffraction limit for the 1.2 m daytime short-exposure high-resolution optical imaging system. The working efficiency of the optical system was improved because the imaging period is extended to 8 h during the daytime, and an image resolution of higher than  $0.4''$  was achieved.

## 1 Bent Cassegrain system

Fig.1 shows the bent Cassegrain configuration that was applied to the 1.2 m active optical system. The light from an infinite target is reflected by the mirrors M1 and M2 to the planar reflector M3<sup>[11-12]</sup>. M3 then reflects the light to the bent Cassegrain focus, which connects the telescope and daytime high-resolution optical system. This system can collect optical energy with a large aperture and deliver the light beam in the optical system. It also provides a wavefront beam with good field quality. The bent Cassegrain-based active optical system has the following advantages; a short optical path, movable observation, and no image rotation. Table 1 presents the optical parameters of the bent Cassegrain-based active optical system.

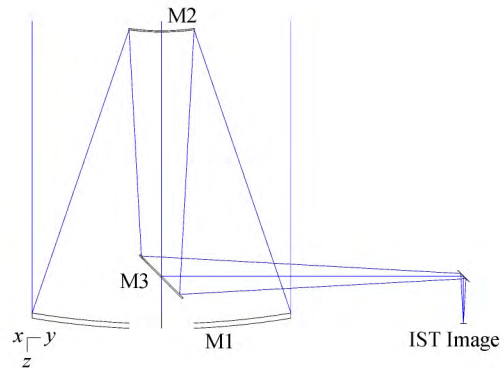


Fig.1 Optical layout of the Cassegrain focal optical system

**Table 1** Parameters of the active optical system

Optical parameters	Required index
Aperture	1 200 mm
Focal length	15 mm
Field of view	$6'$
Obscuring ratio	$<5\%$
Spectral range	700~1 700 nm

## 2 Daytime high-resolution optical imaging system

### 2.1 Sky background analysis

As we know, sunlight and the radiation of the target are the light sources of the target image. Therefore, the reflection luminance and radiation intensity of the target are determined by the orbital height of the target<sup>[13-15]</sup>, location of the observation station, and relative positions of the target and Sun.

In the near-infrared visible waveband, sunlight is the main light source for imaging a space target. The magnitude of a satellite, which depends on the orbital height, can be calculated as follows

$$M_v = 1 - 26.74 - 2.5 \log_{10}[A\rho F(\varphi)] + 5.0 \log_{10}(R) \quad (1)$$

where  $A$  is the cross-sectional area of the effective target reflection,  $\rho$  is the reflectivity of the target,  $R$  is the observed slant distance of the target, and  $F(\Phi)$  is the phase angle function. If the space target is assumed to be a diffused cylinder, its phase angle function can be specified as

$$F(\varphi) = \frac{1}{4\pi} [(\pi - \varphi)\cos \varphi + \sin \varphi] \quad (2)$$

Thus, the magnitude of a target is influenced by the sky background and elevation angle. In this work, the space target (i.e., a cabin with a length of 10 m and diameter of 3.5 m) is represented as a diffused cylinder with a cross-sectional area of 35 m<sup>2</sup>. The elevation angle dependence of the magnitude is shown in Fig.2, where the different line style corresponding to different phase angles. To obtain these results, we set the observed distance of the space target from 340 km to 1 270 km and the surface reflectivity to 0.6. We also considered the influence of the atmospheric transmittance. The luminance of the space target had a magnitude of greater than 2.5 with a phase angle of less than 90° and elevation angle of greater than 30°.

The atmosphere is the main factor that influences the transmitting path of photons because of the background formed by atmospheric radiation, atmospheric extinction, atmospheric refraction, and atmospheric turbulence<sup>[16]</sup>. The atmospheric extinction is the reduction in brightness of the space target as its photons pass through the atmosphere. The wavelength dependence of the atmospheric transmission is shown in Fig.3, where the curves correspond to different zenith angles. Different atmosphere windows—which include visible light, near-infrared light, short-wavelength infrared light, middle-wavelength infrared light, and long-wavelength infrared light—are induced by atmospheric extinction. The I, J, H, L, and M atmosphere windows were chosen to realize imaging space target with multiple wavebands. Because the effect of atmospheric extinction decreases as the zenith angle increases, the signal-to-noise ratio of imaging is obviously high at large elevation angles.

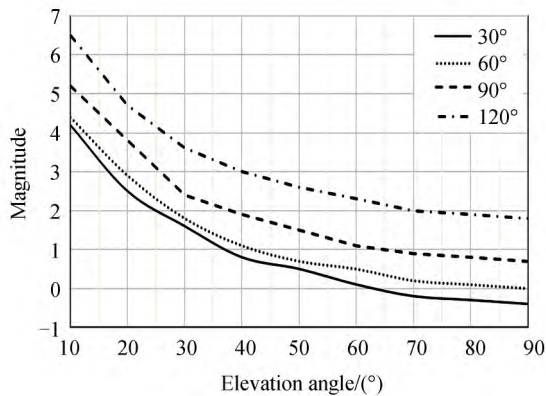


Fig.2 Relationship between the target's magnitude and elevation angles of the observation

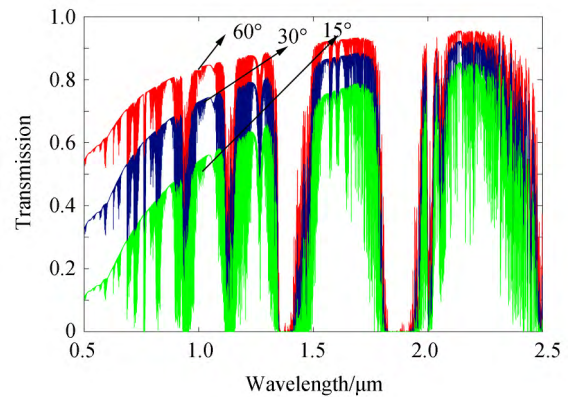


Fig.3 Changes in the atmospheric transmittance with respect to the zenith angle

The AEOS telescope measured the sky background radiation and indicates that stray radiation changes with time. This indicates that the influence of atmospheric scattering increases with the elevation angle. Furthermore, wavebands less than 600 nm are significantly scattered. Therefore, the influence of atmosphere on the background can be reduced by choosing a waveband larger than 600 nm for daytime tilt correction and imaging.

## 2.2 Optical system layout

The daytime high-resolution optical imaging system is fixed on the bent Cassegrain focus of the 1.2 m telescope. As shown in Fig.4, the gathered light beam, which is reflected from the planar reflector M3 (see Fig.1), is collimated by the relay optical system. After split-spectrum processing, the light beam then travels into the precise tracking and tilt correction system and high-resolution double-pass imaging system. The relay optical system collimates the light gathered by the active optical system into parallel light, which provides an exit pupil that matches the tip-tilt mirror in the tilt correction system<sup>[17-20]</sup>. The short-wavelength infrared light (0.9~1.7 μm) is reflected into the tilt correction system by CS1, which is a

critical component for split-spectrum processing. At the same time, near-infrared light ( $0.7 \sim 0.9 \mu\text{m}$ ) passes through CS1 and is then split based on the energy by the spectroscope BS in the double-pass high-resolution imaging system. Therefore, the daytime double-pass optical system realizes pupil relay, atmospheric wavefront tilt correction, and high-resolution imaging with various wavebands.

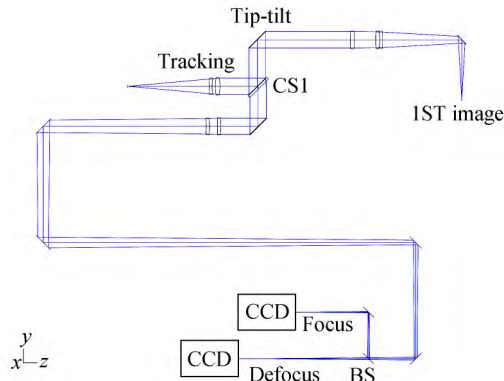


Fig.4 Layout of the daytime resolution imaging system

### 2.3 Tilt detection and correction

The atmospheric turbulence influences the imaging quality of a telescope in two ways: the global wavefront tilt and local wavefront distortion. According to the Kolmogorov atmospheric turbulence theory, when 2.5 standard deviations of the normal distribution covers about 98.4% of the range, the global atmospheric wavefront tilt can be expressed as

$$\Delta_{tt} = \pm 2.5 \sqrt{0.182 \cdot (D/r_0)^{5/3} \cdot (\lambda/D)^2} \text{ rad} \quad (3)$$

For a 1.2 m telescope, when  $r_0$  is 7 cm, the atmospheric tilt is

$$\Delta_{tt} = \pm 2.5 \sqrt{0.182 \cdot (D/r_0)^{5/3} \cdot (\lambda/D)^2} \text{ rad} = \pm 2.5'' \quad (4)$$

In addition to the atmospheric global wavefront tilt, the system also has residual tracking errors that can show up in the wavefront tilt of the entrance pupil. Because the wavefront tilting caused by the residual tracking errors of the 1.2 m telescope is less than  $\pm 5''$ , the correction of the global wavefront tilt at the entrance pupil of the telescope is

$$\delta = \pm \sqrt{(5^2 + 2.7^2)} = \pm 5.7'' \quad (5)$$

Therefore, the tilt detection and correction system mainly measures and corrects two kinds of tilt: the global atmospheric wavefront tilt and wavefront tilt caused by residual tracking errors of the system. These two functions are fulfilled by a closed loop of detection and correction that comprises the tip/tilt mirror, CS1, T-lens, and detector. According to the object amplification relationship, the magnification of the tip/tilt mirror is  $m = 1200/40 = 30$ . Therefore, the distance of the tip/tilt mirror is

$$\delta' = \pm 5.7'' \times 30 = \pm 171'' = \pm 2.85' \quad (6)$$

The tip/tilt mirror and entrance pupil of the system should completely match each other conjugately. Table 2 presents the parameters of the tilting mirror.

Table 2 Parameters of the tilting mirror

Tip/tilt mirror component type	Plane mirror
Surface accuracy	10 nm (RMS)
Stroke	$\pm 200''$
Clear aperture	40 mm

The optical parameters of the tilt detection and correction system were obtained as follows: a pixel sensitivity of  $0.5'' \sim 1''$ , working waveband of  $0.9 \sim 1.7 \mu\text{m}$ , field of view of  $2'$ , and distance of the tip/tilt mirror of  $\geq |3'|$ . In this tilt detection and correction system, the global wavefront tilt at the entrance pupil is detected and corrected by splitting the spectrum.

### 2.4 Double-pass imaging system

The atmospheric turbulence influences the imaging quality of a telescope in two ways: the global wavefront tilt and local wavefront distortion. According near-diffraction-limited high-resolution imaging is

achieved with the double-pass imaging system, which is where the light beam corrected by the tilt correction system. According to the Rayleigh criterion, the diffraction-limited angular resolution for the waveband of 700~900 nm using the 1.2 m telescope is

$$\epsilon = 1.22 \frac{\lambda}{D} = 1.22 \times \frac{0.8}{1200} = 0.168'' \quad (7)$$

Therefore, the imaging system should be an optical system with a large F number. Table 3 presents the parameters of the high-resolution imaging system. The Full Width at Half Maximum (FWHM) was used to measure the resolution of the near-diffraction-limited optical systems. The Root Mean Square (RMS) wave aberration of the system in the field range was better than  $\lambda/60$ .

**Table 3 Optical parameters of the imaging system**

Optical parameters	Required index
Clear aperture	1 200 mm
Focus length	70 m
Field of view	40''
FWHM	Superior to 0.2''
Wavelength region	700~900 nm

### 3 Phase-diversity speckle technique

Fig.5 illustrates the main principle of the Phase-Diverse Speckle (PDS) technique. Two Charge-Coupled Device (CCD) cameras (of the same model) are placed on the focal and off-focus planes, respectively, while a beam splitter is set on the original light path to generate a known defocusing distance<sup>[21-22]</sup>. Multi-frame data of the object are collected in pairs at the same time, while the collection time is controlled by the same external trigger pulse. In order to clarify the image, the information of the instantaneous optical wavefront is estimated with the Fourier optical principle, and the closest solution to the real image is obtained by applying the inverse filtering and optimization method.

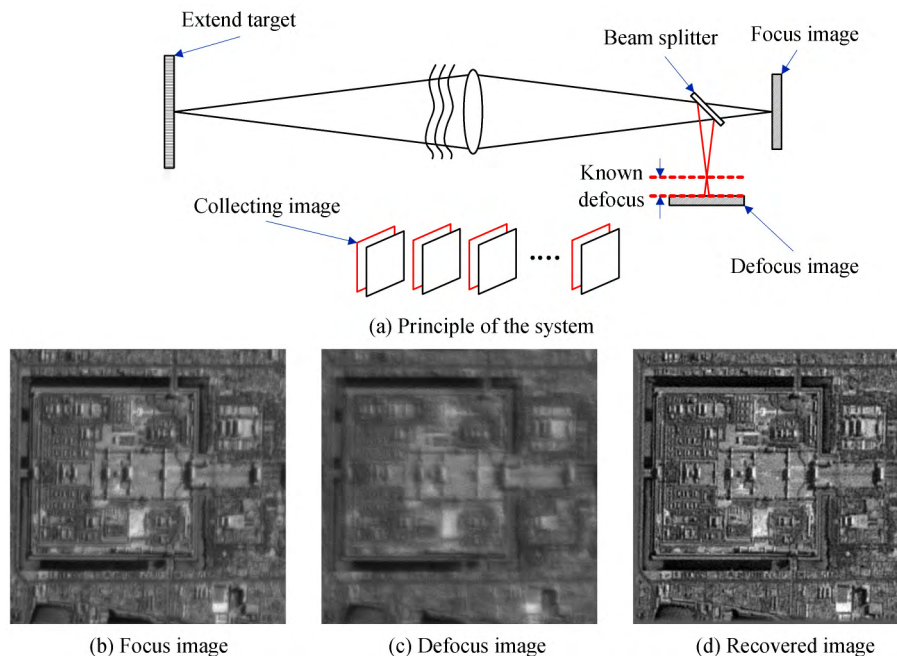


Fig.5 Principle of the phase-diversity technique

The principle of PSD image restoration is based on the assumption that the noise distribution of the camera follows a Gaussian distribution. An evaluation function is built to express the relationship between the actual target and ideal target. Then, an evaluation function unrelated to the target is obtained by using the maximum likelihood to estimate a separate target as an independent intermediate step from phase estimation. Thus, image restoration can be described as a nonlinear optimization process for seeking extrema. Wavefront information and the ideal image can be obtained by applying various optimization

methods, including the limited-memory quasi-Newton code for bound-constrained optimization (L-BFGS-B).

The basic mathematical model for PSD restoration assumes that the atmosphere and telescope are a linear and space-invariant system. With an incoherent light source, imaging with the Gaussian noise model is given by

$$d(x) = f(x) * s(x) + n(x) \quad (8)$$

where  $d$  is the target image collected from CCD,  $f$  is the ideal image of the target,  $s$  is the point spread function,  $n$  is the Gaussian noise, and  $x$  is the image coordinate. Under the near-field condition, the point spread function can be expressed as

$$s(x) = |F^{-1}\{P(v)e^{i\varphi(v)}\}|^2 \quad (9)$$

where  $F^{-1}$  is the inverse Fourier transform,  $v$  is the pupil surface coordinate, and  $P$  is the pupil function. Here,  $\varphi$  is the wavefront phase that can be decomposed into a group of the sum of Zernike polynomials

$$\varphi(v) = \theta(v) + \sum_{m=4}^M a_m z_m(v) \quad (10)$$

where  $a_m$  is the polynomial coefficient,  $z_m$  is the base of Zernike polynomials, and  $\theta$  is a known constant corresponding to the defocus phase.

Based on the Gaussian noise model, the mean square of the target and multi-channel image can be used as the following likelihood function for the frequency domain

$$L(f, \{a\}_t) = \frac{1}{2N} \sum_u \left( \sum_{t=1}^T \sum_{c=1}^C |D_{tc}(u) - FSt_c(u)|^2 + \gamma |F(u)|^2 \right) \quad (11)$$

where  $u$  is the coordinate in the frequency domain;  $T$  is the number of frames;  $C$  is the number of channels;  $N$  is the total number of pixels in a single image;  $\{a\}_t$  is the Zernike polynomial coefficients of  $t$  frame that needs to be solved; and  $D(u)$ ,  $F(u)$ , and  $S(u)$  correspond to the actual target image, idealistic target image, and point spread function, respectively, for the frequency domain after the Fourier transform. The second term in brackets is the Tikhonov canonical term, which improves the stability and convergence speed of the algorithm, while  $\gamma$  is a non-negative coefficient.

According to the maximum likelihood estimation, the target estimation can be separated as an independent intermediate step from the phase estimation<sup>[23-24]</sup>. By differentiating Eq. (9) with respect to the Fourier transform of the ideal target image  $F(u)$  and evaluating it at 0, we can obtain an evaluation function that is unrelated to the target, as shown in Eq. (11). With this evaluation function, image restoration can be described as a nonlinear optimization process for seeking extremum. This process can be used to obtain the optimum Zernike polynomial coefficients with an appropriate searching algorithm and then estimate a clear ideal image.

## 4 System integration testing and imaging

### 4.1 System integration testing

As shown in Fig. 6, the daytime optical imaging system was integrated and tested in lab. The test included wave aberrations, simulated imaging with white light, and aberration of the phase diversity.

The precise tracking and tilt correction system employed a short-wavelength infrared camera with the following parameters: a waveband of  $0.9 \sim 1.7 \mu\text{m}$ , resolution of  $640 \text{ pixel} \times 512 \text{ pixel}$ , and pixel size of  $20 \mu\text{m}$ . The double-pass high-resolution imaging system employed a DV887 camera with the following parameters: a waveband of  $0.7 \sim 0.9 \mu\text{m}$ , resolution of  $512 \text{ pixel} \times$

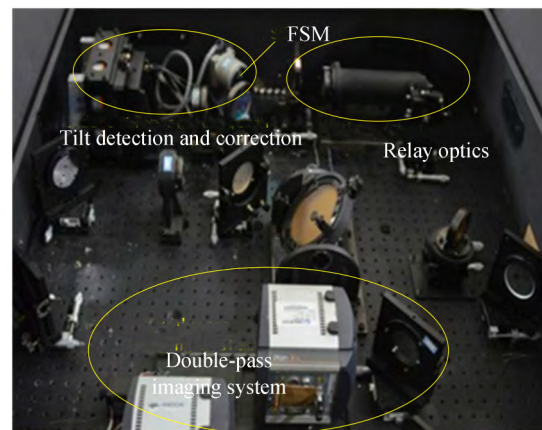


Fig.6 Indoor integrated daytime imaging system

512 pixel, and pixel size of  $16 \mu\text{m}$ . As shown in Fig.7, we used a dynamic interferometer to test the auto-collimation of the wave aberrations of the relay optical system, precise tracking and tilt correction system, and double-pass imaging system.

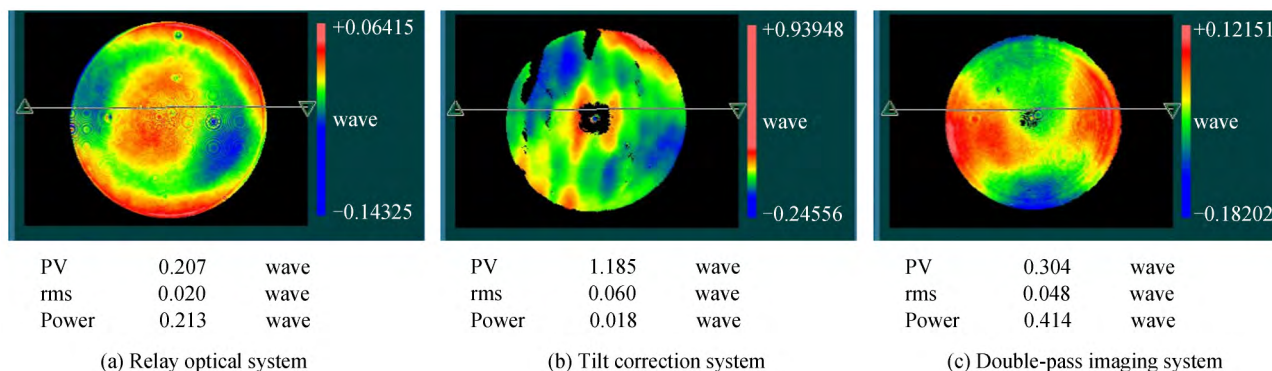


Fig.7 Testing results for wave aberrations of systems

## 4.2 Stellar object imaging

In order to test the ability of the daytime imaging system on the telescope, we used a completely tested 1.2 m telescope-based daytime imaging system during the daytime to observe stars.

### 4.2.1 Imaging of a stellar object

At 10 : 03 am on August 14, 2016, we imaged a stellar object with a magnitude of 4.32. Fig.8 shows the original image taken by a camera and the image restored with the phase-diversity technique. The comparison of the two images shows that most of the atmospheric wavefront distortion was corrected. The imaging FWHM was  $0.352''$ , and the resolution was close to twice the diffraction limit when the precise tracking and tilt correction system was used with wavefront phase-diversity restoration.



Fig.8 Images of the stellar object with the phase-diversity technique

### 4.2.2 Imaging of a double star

At 15 : 22 pm on April 11, 2016, a double star was imaged with the precise tracking and tilt correction system and wavefront phase-diversity restoration. Fig.9 shows the results. The magnitudes of the two stars were 5.33 and 5.62, respectively, while the distance between them was  $0.4''$ . The resolution of the restored image was close to twice the diffraction limit.

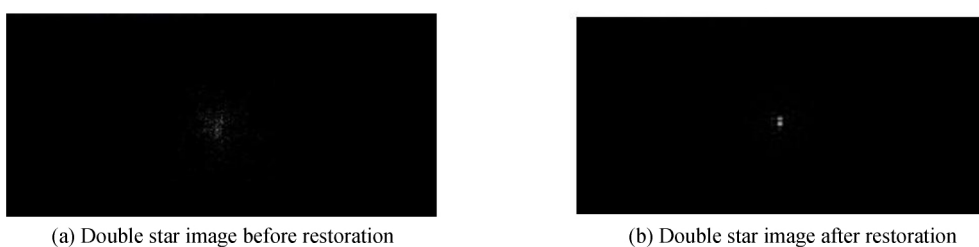


Fig.9 Images of the double star with the phase-diversity

## 4.3 Imaging of the international space station

At 10 : 55 am on October 22, 2015, precise tracking, tilt correction, and phase-diversity imaging restoration were applied to imaging the International Space Station. The elevation angle of observation was  $28.5^\circ$ . As shown in Fig. 10, the image resolution was significantly improved.



Fig.10 Images of the ISS (left) before and (right) after restoration with the PD technique

#### 4.4 Imaging results and analysis

The residual aberration of the optical system can be calculated by using the resolution of the system, which is represented as

$$\sigma = \frac{2\pi}{\lambda} \varphi \quad (12)$$

where  $\alpha$  is the wave aberration of the system in radians and  $\varphi$  is the wave aberration of the system in terms of the wavelength. The Strehl ratio of the system is given by

$$\text{Strehl} = \begin{cases} \exp(-\sigma^2) & 0 \leq \sigma^2 \leq 0.059 \text{ rad}^2 \\ 0.99689 - 0.9451\sigma^2 + 0.5765\sigma^4 - 0.21248\sigma^6 + 0.04162\sigma^8 & 0.059 \text{ rad}^2 \leq \sigma^2 \leq 4 \text{ rad}^2 \\ -0.00328\sigma^{10} & 0.059 \text{ rad}^2 \leq \sigma^2 \leq 4 \text{ rad}^2 \\ 0.5712\sigma^2 & 4 \text{ rad}^2 \leq \sigma^2 \end{cases} \quad (13)$$

Therefore, the angular resolution of the system is

$$\text{resolution} = 1.22 \left( \frac{\lambda}{D} \right) \frac{1}{\sqrt{\text{Strehl}}} \quad (14)$$

Under the influence of general atmospheric distortion, the resolution is  $1''$ . According to Eqs. (12) and (13), the Strehl ratio is 0.023, and the rms wave aberration of the system is  $0.366\lambda$ . And the resolution of single stellar is  $0.352''$ , So the Strehl ratio is 0.27, and the rms wave aberration of the system is  $0.175\lambda$ .

It is proved that the resolution of 1.2m vehicular daytime imaging system (VDIS) has been improved from  $1''$  to  $0.352''$ , which is near 3 times. And the rms wavefront error has been corrected from  $0.366\lambda$  to  $0.175\lambda$ , which is near 2.2 times.

Now, there are also some factors that influence the image resolution of 1.2 m VDIS: Firstly, atmospheric wavefront distortion includes global wavefront distortion and high-order wavefront distortion. Tilt correction system only corrects global wavefront distortion. The remaining high-order wavefront distortion needs adaptive optical system to correct. Secondly, even with the stray light suppression design, the daytime solar stray light still has a great impact on the imaging signal-to-noise ratio, which makes the imaging resolution of the system reduced and the detection ability decreased. Finally, 1.2 m vehicle-borne telescope is located in the strongest position of atmospheric turbulence on the surface, which has a great influence on imaging resolution.

## 5 Conclusion

The daytime imaging system can reduce the atmospheric wavefront distortion by over 50% and significantly improve the image resolution. Considering the practical results of the integration testing and imaging of the vehicular daytime imaging system based on a 1.2 m optical telescope, we conclude the following: 1) Up to 50% of the atmospheric wavefront distortion can be corrected with the precise tracking and atmospheric global wavefront correction, while using the phase-diversity technique for imaging the near-infrared waveband results in a resolution close to twice the diffraction limit; 2) Because the daytime imaging system can be moved with telescope, high-resolution imaging can be achieved at different observation stations, longitudes, latitudes, and atmospheric visibility; 3) The work efficiency is improved because the daytime imaging system can work from 8 am to 11 am and from 1 pm to 5 pm, which extends the daytime working time by 6 h.

## References

- [1] MA Xin-xue, WANG Jian-li. Surface testing with phase diversity method[J]. *Optics and Precision Engineering*, 2015, **23**(4): 975-981.
- [2] DEAN B, BROWERS C. Diversity selection for phase-diverse phase retrieval[J]. *Journal of the Optical Society of America A*, 2003, **20**(8): 1490-1504.
- [3] BELEN M, BRINKLEY T, BRUNS D, et al. Portable daytime differential image motion sensor for atmospheric turbulence characterization[C]. SPIE, 2010, **7814**: 78140J.
- [4] ZHANG R, XIAN H, RAO C, et al. Study on application of spectral filter in detecting stars in daytime[C]. SPIE, 2012, **8419**: 84190T.
- [5] ZHANG R, XIAN H, RAO C, et al. Study on effect of polarization for improving signal noise ratio of stellar objects in daytime[C]. SPIE, 2011, **8191**: 81911M.
- [6] WEI Pei-feng, LU Zhen-wu, LIU Xin-yue, et al. Performance analysis of adaptive optical system for spatial objectives [J]. *Acta Photonica Sinica*, 2015, **44**(7): 0701001.
- [7] MARCO J, MONTOYA L, COLLADOS M, et al. Daytime turbulence profiling for EST and its impact in the solart MCAO system design[C]. SPIE, 2016, **9909**: 99096X.
- [8] TAN Bi-tao, CHEN Hong-bin, WANG Ji-hong, Image quality evaluation on extended imaging of telescopes[J]. *Acta Photonica Sinica*, 2015, **44**(9): 0911003.
- [9] ZHANG S, WU Y, ZHAO J, et al. Astronomical image restoration through atmosphere turbulence by lucky imaging [C]. SPIE, 2011, **8009**: 80090B.
- [10] MARITZ B, KOAGO M, WAINMAN C, et al. Vertical atmospheric variability measured above water during the FESTER experiment; first results[C]. SPIE, 2016, **10002**: 100020B.
- [11] LIU Xiang-yi, ZHANG Jing-xu, WU Xiao-xia, et al. Affect of environment on mirror seeing of large-aperture SiC lightweight primary mirror[J]. *Optics and Precision Engineering*, 2015, **23**(3): 776-783.
- [12] MING Ming, LV Tian-yu, SHAO Liang, et al. Image restoration and optical test by using offner optical system[J]. *Chinese Optics*, 2012, **5**(6): 646-651.
- [13] JU G, YAN C, GU Z, et al. Aberration fields of off-axis two-mirror astronomical telescopes induced by lateral misalignments[J]. *Optics Express*, 2016, **24**(21): 24665.
- [14] YUE Dan, XU Shu-yan, NIE Hai-tao, et al. Error analysis and eliminate methods for wavefront detection based on phase diversity algorithm[J]. *Acta Optica Sinica*, 2016, **36**(1): 011003.
- [15] RAO C, ZHU L, RAO X, et al. 37-element solar adaptive optics for 26-cm solar fine structure telescope at Yunnan Astronomical Observatory[J]. *Chinese Optics Letters*, 2010, **8**(10): 966-968.
- [16] LAN Bin, YANG Hong-bo, WU Xiao-xia, et al. Influence of unsteady wind loads on imaging quality of the 1.2m ground telescope[J]. *Laser Optoelectronics Progress*, 2016, (53): 111103.
- [17] SCHMIDT D, RIMMELE T, MARINO J, et al. A review of solar adaptive optics[C]. SPIE, 2016, **9909**: 99090x.
- [18] WANG Bin, WANG Zong-yang, WU Yuan-hao, et al. Calibration of no-common path aberration in AO system using multi-channel phase-diversity wave-front sensing[J]. *Optics and Precision Engineering*. 2013, **21**(7): 1683-1692.
- [19] BENJAMIN L, CHRISTIAN M, RAPHAEL G, et al. Fast focal plane wavefront sensing on ground-based telescopes [C]. SPIE, 2018, **10703**: 1070351.
- [20] SCHMIDT D, BERKEFELD T, FEGER B, et al. Latest achievements with the MCAO testbed for the GREGOR solar telescope[C]. SPIE, 2010, **7736**: 773607.
- [21] HERRIOT G, ANDERSEN D, ATWOOD J, et al. NFIRAOS: TMT's facility adaptive optics system[C]. SPIE, 2010, **7036**: 77360B.
- [22] MARK T, BRETT A, MICHAEL B, et al. Adaptive spatial filtering for daytime satellite quantum key distribution[C]. SPIE, 2014, **9254**: 925404.
- [23] HU Jin-jin, LIU Jing, CUI Shuang-xing, et al. Evaluation model of detected ability for ground-based electro-optic telescope to space debris[J]. *Acta Photonica Sinica*, 2016, **45**(10): 1012002.
- [24] CHENG Qiang, XUE Dong-lin, Realizing assisted alignment of three-mirror reflecting optical system by using wavefront sensing test results of phase diversity[J]. *Acta Optica Sinica*, 2016, **36**(7): 0711005.